

Full length article

Accelerating the identification of stable configurations in mixed-anion perovskite materials

Chunwei Zhu, Xiaotong Yan, Yu-Jie Cen, Chang-Chun He, Yu-Jun Zhao, Xiao-Bao Yang*

School of Physics and Optoelectronics, South China University of Technology, Guangzhou, 510640, Guangdong, People's Republic of China

ARTICLE INFO

Keywords:

Perovskite
Stable structures
The first-principles calculations
Cluster expansion
Atom classification model

ABSTRACT

Mixed-anion perovskite materials exhibit tunable properties, such as band gaps, stability, and charge transport, by modulating the composition and arrangement of the anions. This tunability enables a wide range of applications in fields such as optoelectronics, catalysis, and energy storage. The structural diversity enriches the material properties and enhances performance; however, it also poses a significant challenge in determining stable structures. The stability of such alloy materials depends not only on the elemental composition but also on the arrangement of X/Y elements within the lattice. To improve the understanding of the structure–property relationship in these alloy systems, a thorough exploration of the vast compositional and configurational space is essential. Herein, we integrate the cluster expansion (CE) method with the atom classification model (ACM) to efficiently pre-screen candidate structures and identify stable configurations. By considering the arrangement of anions, which exhibit short-range ordering within octahedra and randomness between octahedra, we have designed correlation functions for the ACM to reasonably reflect these characteristics. This approach enabled us to identify configurations of $\text{BaTa}(\text{O}_{1-x}\text{N}_x)_3$, $\text{RbPb}(\text{F}_{1-x}\text{O}_x)_3$ and $\text{CsPb}(\text{Br}_{1-x}\text{Cl}_x)_3$ with higher stabilities without significantly increasing computational costs.

1. Introduction

Perovskites, characterized by the general formula ABX_3 , are a widely studied group of compounds due to their excellent material properties [1–9]. The perovskite structure can be described as a three-dimensional arrangement of BX_6 octahedra, where the X-site represents the anion position and can be occupied by elements such as halides, sulfur, oxygen, or nitrogen. The B-site is typically occupied by metal cations capable of forming octahedral coordination (e.g., Pb^{2+} , Sn^{2+} , or Ta^{4+}), while the A-site is generally filled by cations accommodated in the cavities formed by interconnected BX_6 octahedra via shared vertices. These cations may be organic (e.g., MA^+ , FA^+) or inorganic (e.g., Cs^+ , Rb^+ , Ba^{2+}) [7,10–12].

Despite the broad applicability of perovskites in various fields, the number of experimentally accessible ternary systems remains limited. Many systems encounter critical challenges in practical applications, including high toxicity, a wide band gap for light absorption, and long emission wavelengths [11,13,14]. Alloying is considered an effective strategy to address these issues, offering new degrees of freedom to explore material properties. For instance, substituting a suitable anion Y at the X position forms a mixed-anion alloy system $\text{AB}(\text{X}_{1-n}\text{Y}_n)_3$, enabling precise control over the physical and chemical properties of the material.

Within the $\text{AB}(\text{X}_{1-n}\text{Y}_n)_3$ mixed-anion perovskite alloy system, variations in the effective radii, electronegativity, and oxidation states of the X and Y anions can lead to distinct preferences for anion arrangement patterns across different systems. For example, in the ATaO_2N (A = Ca, Sr, and Ba) system [15–22], computational simulations and experimental measurements have suggested that the cis-configuration, where the two N atoms in the TaO_4N_2 octahedron occupy two adjacent edge positions, is energetically more stable. Conversely, in the SrVO_2H system, the trans-configuration, where the two H atoms in the same VO_4H_2 octahedron occupy opposite vertex positions, is energetically favorable [23]. Furthermore, the anion sequence on the surface of a mixed-anion perovskite material may differ significantly from that in the bulk material [24,25], and strain can alter the preferred ordering of anions in these materials [25–27]. Consequently, identifying the anion sequence in mixed-anion perovskite compounds is highly complex.

To understand the structure–property relationships in mixed-anion perovskite materials, it is essential to determine the stable arrangement of anions within these materials. However, experimental characterization methods are limited, making it challenging to fully resolve the anion sequence experimentally. Computational simulations are thus employed to predict crystal structures and determine stable anion

* Corresponding author.

E-mail address: scxbyang@scut.edu.cn (X.-B. Yang).

arrangement configurations. Directly enumerating the large compositional and configurational space using first-principles approaches is impractical due to the exponential growth in the number of candidate structures as the number of substitutable sites in the crystal structure increases [28], resulting in prohibitively high computational costs. Therefore, an effective strategy is needed to reduce the number of candidate structures and identify stable configurations more efficiently.

In this study, we integrate the cluster expansion (CE) method with the atom classification model (ACM) to classify configurations in mixed-anion perovskite alloy systems without relying on prior first-principles computational data. This approach enables us to employ a step-by-step calculation process to pre-screen ground-state configurations efficiently. Our strategy has been successfully validated in mixed-anion perovskite materials, including CsPb(Br_{1-x}Cl_x)₃, RbPb(F_{1-x}O_x)₃, and BaTa(O_{1-x}N_x)₃.

2. Theoretical methods

2.1. CE method

The core of the CE method involves representing the original system within an ideal lattice framework using a set of cluster functions. These cluster functions allow the properties of interest, which depend on the configurations within the original system, to be expressed as a linear combination. Further details on these cluster functions can be found in previous studies [29–32].

To describe structural stabilities, the locally relaxed energy of a specific configuration, σ , in a binary alloy A_{1-x}B_x can be expressed as the sum of the interactions of clusters:

$$E(\sigma) = N \sum_{\alpha} m_{\alpha} J_{\alpha} \bar{\Pi}_{\alpha}(\sigma) \quad (1)$$

Here, the cluster α refers to a collection of sites within the lattice structure. N represents the number of lattice sites occupied by a mixture of elements. The multiplicity m_{α} is the number of symmetry-equivalent clusters per site. J_{α} represents the effective cluster interaction (ECI) coefficients. $\bar{\Pi}_{\alpha}$ signifies the lattice-averaged cluster correlation function, obtained by multiplying the pseudo-spin variables (denoted as -1 for A atoms and $+1$ for B atoms) at the corresponding lattice sites and averaging these values over all symmetry-equivalent clusters.

$$\bar{\Pi}_{\alpha}(\sigma) = \frac{1}{N m_{\alpha}} \sum_{(i_1 < i_2 < \dots < i_g) \in \alpha} S_{i_1} S_{i_2} \dots S_{i_g} \quad (2)$$

where g represents the number of sites in the α -cluster. When all possible clusters are included in the summation, the expansion in Eq. (1) becomes exact [31]. However, in practice, it is typically truncated to include only a limited number of short-range clusters for computational feasibility. The ECIs are determined by fitting data obtained from density functional theory (DFT) calculations for several tens or hundreds of ordered supercell structures. The performance and predictive accuracy of the truncated cluster expansion model are assessed using the leave-one-out cross-validation (LOOCV) method [33], which is defined as

$$E_{CV} = \sqrt{\frac{1}{N_s} \sum_i (E_i - \hat{E}_{(i)})^2} \quad (3)$$

Here, N_s represents the number of structures, E_i is the energy of the i th structure as directly calculated by DFT, and $\hat{E}_{(i)}$ is the energy of the i th structure predicted by a cluster expansion model that excludes the i th structure from the training dataset.

2.2. Special quasi-random structure (SQS) method

The SQS method, originally proposed by Zunger et al. [34,35], is designed to simulate the structure and properties of randomly

substituted alloys using a small unit cell. In general, the probability of a particular structure appearing is influenced by multiple factors, including its degrees of structural freedom, energy, and temperature. At the high-temperature limit, this probability becomes proportional to the structural degrees of freedom. The primary goal of the SQS model is to construct a specialized small unit cell under periodic boundary conditions that closely replicates the atomic spatial distribution of random alloys in their ideal state. This allows the random alloy structure to be effectively simulated through an organized supercell. The approach of the SQS model relies on the near-neighbor recurrence principle to generate structures that closely mimic the nearest, next-nearest, and other short-range atomic arrangements present in a perfectly random alloy state. This method prioritizes interactions between neighboring atoms, as these are more significant than interactions between distant neighbors. Consequently, periodic errors are shifted to interactions with more distant neighbors, thereby improving the accuracy of the simulation [31,36].

In the SQS method, the key quantity is the cluster correlation functions (CCFs), which are defined as the ensemble average of the cluster function introduced in Eq. (1).

$$\langle \bar{\Pi}_{\alpha} \rangle_T = \frac{\sum_{\sigma} \bar{\Pi}_{\alpha}(\sigma) e^{-\beta E(\sigma)}}{\sum_{\sigma} e^{-\beta E(\sigma)}} \quad (4)$$

For completely random situations, corresponding to the limit as T approaches infinity, the occupancies at different positions become uncorrelated, and the CCFs can be determined analytically [37].

$$\langle \bar{\Pi}_{\alpha} \rangle_{\infty} = \left\langle \prod_{i \in \alpha} S_i \right\rangle = \prod_{i \in \alpha} \langle S_i \rangle = (2x - 1)^g \quad (5)$$

Here, g represents the number of sites in cluster α , while x represents the substitution rate. Eq. (5) provides a quantitative measure of organization, enabling the characterization of orderliness. Smaller deviations of the CCFs from Eq. (5) indicate a higher level of randomness, while larger deviations suggest a greater degree of orderliness.

2.3. ACM

In our recent study [38], we proposed an ACM to describe multi-component materials based on structural recognition. To illustrate this, consider a simple system with nearest-neighbor (NN) interactions. The Hamiltonian for the lattice gas model (LGM) [39] is expressed as

$$\begin{aligned} H_{LGM} = & - \sum_i (\mu_A P_i^A + \mu_B P_i^B) \\ & - \sum_{\langle NN \rangle} [J_{AA} P_i^A P_j^A \\ & + J_{AB} (P_i^A P_j^B + P_i^B P_j^A) + J_{BB} P_i^B P_j^B] \end{aligned} \quad (6)$$

where μ_A and μ_B represent the chemical potentials of atoms of types A and B, respectively. J_{AA} , J_{AB} , J_{BB} denote the strengths of NN interactions for A–A, A–B, and B–B bonds, respectively. P_i^A and P_i^B indicate the occupation status of A and B atoms at the i th lattice site, with 1 representing occupation and 0 representing non-occupation. After normalizing the coefficients, the correlation functions can be expressed as follows:

$$\begin{aligned} \Pi_{LGM} = & \frac{1}{N} \left(\sum_i P_i^A, \sum_i P_i^B, \sum_{\langle NN \rangle} P_i^A P_j^A, \sum_{\langle NN \rangle} (P_i^A P_j^B \right. \\ & \left. + P_i^B P_j^A), \sum_{\langle NN \rangle} P_i^B P_j^B \right) \end{aligned} \quad (7)$$

Here, N denotes the number of lattice sites, which serves as a normalization constant.

Introducing the variable S_i , where $S_i = 1$ (or -1) denotes an A (or B) atom being occupied at site i , we have:

$$\begin{aligned} P_i^A &= \frac{1}{2}(1 + S_i) \\ P_i^B &= \frac{1}{2}(1 - S_i) \end{aligned} \quad (8)$$

Using this substitution, formula (6) can be rewritten as

$$\begin{aligned}
 H_{\text{LGM}} = & -\frac{N}{2}(\mu_A + \mu_B) - \frac{1}{2}(\mu_A - \mu_B) \sum_i S_i \\
 & - \frac{1}{4} J_{AA} \left[\sum_{\langle \text{NN} \rangle} (1 + S_i S_j) + \alpha \sum_i S_i \right] \\
 & - \frac{1}{2} J_{AB} \left[\sum_{\langle \text{NN} \rangle} (1 + S_i S_j) \right] \\
 & - \frac{1}{4} J_{BB} \left[\sum_{\langle \text{NN} \rangle} (1 + S_i S_j) + \alpha \sum_i S_i \right]
 \end{aligned} \quad (9)$$

Here, α depends on the number of NN atoms and varies based on the lattice and dimensionality. The resulting Hamiltonian can then be expressed as the ACM.

$$\begin{aligned}
 H_{\text{ACM}} = & J_1(\mu_A, J_{AA}, \alpha) \sigma_i^1 \left(\sum_i S_i, \sum_{\langle \text{NN} \rangle} S_i S_j \right) \\
 & + J_2(\mu_A, \mu_B, J_{AB}, \alpha) \sigma_i^2 \left(\sum_i S_i, \sum_{\langle \text{NN} \rangle} S_i S_j \right) \\
 & + J_3(\mu_B, J_{BB}, \alpha) \sigma_i^3 \left(\sum_i S_i, \sum_{\langle \text{NN} \rangle} S_i S_j \right)
 \end{aligned} \quad (10)$$

The correlation functions of the ACM can be represented as

$$\Pi_{\text{ACM}} = \frac{1}{N} (\sigma_i^1, \sigma_i^2, \sigma_i^3) \quad (11)$$

Here, new parameters J_1, J_2, J_3 are introduced as functions of $\mu_A, \mu_B, J_{AA}, J_{AB}, J_{BB}, \alpha$, respectively. These correlation functions can be calculated as a function of $\sum_i S_i$ and $\sum_{\langle \text{NN} \rangle} S_i S_j$, ensuring non-negative values after the transformation. Additionally, if the selection of the largest multi-body clusters within a truncated radius is exhaustive in the LGM, terms corresponding to smaller clusters can be linearly represented by these largest multi-body clusters. Thus, the information from smaller cluster terms becomes redundant. Consequently, the Hamiltonian of the system can be fully expanded using only multi-body clusters.

Generally, various interaction parameters influence the stability of alloy systems, and stable structures often depend on the alloying composition. Notably, the convex point vectors in the vector space of correlation functions correspond to the extrema of the Hamiltonian, thereby guiding the selection of stable configurations. Consequently, possible configurations under different substitution systems can be generated using convex point templates within the same lattice structure. It is important to highlight that an ACM template configuration, which may not represent a true convex point in one system, could indeed serve as a true convex point configuration in another system. This approach proves useful for identifying stable configurations in structurally similar systems and strategically prioritizing calculations based on the number of non-zero components in the correlation function vector, enabling an efficient step-by-step search for stable configurations.

To identify the most stable configurations in alloy systems, ACM significantly reduces the number of candidate structures while providing a systematic strategy to accelerate the determination of stability. This method establishes a direct structure-stability correlation, revealing the predominant influence of geometric symmetry on structural stability. Specifically, structures with fewer components in the correlation function are more likely to emerge as ground states.

2.4. Computational details

The workflow for identifying stable configurations is illustrated in Fig. 1(a), and the detailed computational procedures executed in this study are outlined below. First, we used the CsPbBr₂Cl system as an example to explore the ordering of anions within the perovskite lattice. The energies of a set of non-equivalent configurations of CsPbBr₂Cl were calculated using first-principles methods. A cluster expansion model was then constructed to estimate the ground-state energy, and

Monte Carlo sampling was employed to evaluate CCFs at finite temperatures to analyze anion ordering. Based on the observed ordering characteristics, the ACM was applied to design rational correlation functions, categorizing non-equivalent configurations and identifying potentially stable configurations. Finally, a comparative validation of the stability of the identified configurations was performed within several commonly reported perovskite alloy systems.

As previously reported in the literature [11,16,40], the cubic perovskite structure with the space group symmetry of Pm $\bar{3}$ m was employed in this study for simulations. To construct the cluster expansion of the energy, we generated 163 structures from the $2 \times 2 \times 2$ supercell (40-atom) of the cubic primitive cell of CsPbBr₂Cl. The first-principles calculations were performed based on DFT using the Vienna Ab initio Simulation Package (version 5.4.4) [41,42], incorporating the projector-augmented-wave (PAW) method [43] to treat the valence-core interactions. Valence electron configurations of the atoms are Br-4s²4p⁵, Cl-3s²3p⁵, Cs-5s²5p⁶6s¹, Pb-5d¹⁰6s²6p², O-2s²2p⁴, Rb-4s²4p⁶5s¹, F-2s²2p⁵, N-2s²2p³, Ta-5p⁶5d³6s², Ba-5s²5p⁶6s², respectively. The cutoff energy for the plane wave basis functions was set to 520 eV, and Γ -centered k-point meshes with a grid spacing of $0.02 \times 2\pi \text{\AA}^{-1}$ were employed for Brillouin zone sampling. The Perdew–Burke–Ernzerhof (PBE) functional was used to describe the exchange–correlation interaction [44]. The atomic positions and cell size were fully relaxed for each configuration. Geometric optimization was halted when the residual atomic forces on the atoms dropped below 0.01 eV/Å, and the final energies were calculated in a subsequent static calculation. All inequivalent configurations were obtained using the SAGAR package with the Hermite normal form matrices [45,46].

We conducted Monte Carlo simulations on a $20 \times 20 \times 20$ supercell using the emc2 module from ATAT [47,48]. The number of equilibration and sampling steps was determined following the algorithm outlined in a previous study [49]. The target tolerance for the statistically averaged energy was set to 1×10^{-5} eV, which is sufficient to ensure the numerical convergence of the CCFs.

3. Results and discussion

3.1. Cluster expansion for the CsPbBr₂Cl system

To enhance the efficiency of screening stable structures, energy evaluation can be simplified by adopting an interaction model. Detailed information on constructing the optimal cluster expansion model for energy and its validation is provided in Fig. S1 (see Supporting Information). The two-body clusters considered in the optimal model are depicted in Fig. 1(b). Monte Carlo simulations were employed to analyze the variations in two-body CCFs at finite temperatures based on the cluster expansion model. The dashed lines in Fig. 1(c) indicate the CCF values for Br and Cl in the CsPbBr₂Cl system under a completely random distribution, as determined using the SQS method and Eq. (5). With the exception of the 3rd cluster, the CCFs for the other two-body clusters rapidly approach values indicative of a completely random distribution as temperature increases. However, the 3rd cluster exhibits a significant deviation from randomness, even at a high temperature of 1000 K. This suggests that Br and Cl are not randomly distributed but display short-range order. Furthermore, the presence of the 3rd cluster within individual octahedra indicates short-range order within octahedra, whereas the distribution of anions between octahedra remains relatively random. This observation aligns with previous studies on the distribution of O and N in the BaTaO₂N system [51]. Considering the arrangement of anions and the characteristics of the ACM, configuration correlation functions can be constructed based on octahedral many-body clusters. By conducting a convex point-solving process in the correlation function space for all configurations within the system [38], the formation energy calculations are prioritized for configurations where the correlation function corresponds to a convex point. This approach significantly accelerates the search for stable configurations.

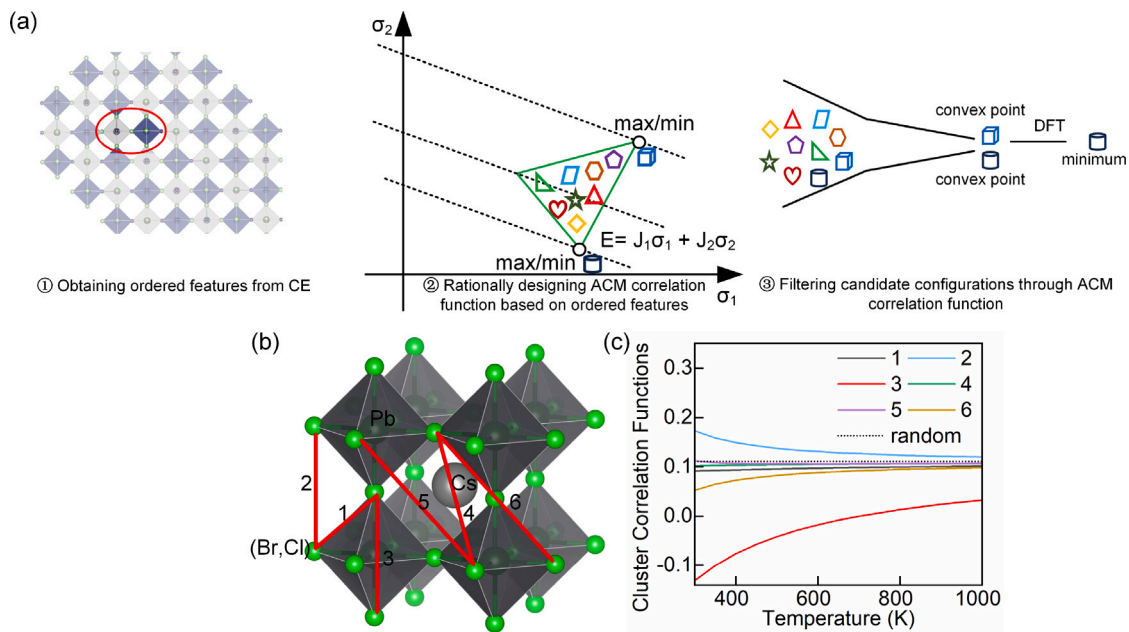


Fig. 1. (a) Workflow for the identification of stable mixed-anion perovskite structures. (b) Six inequivalent two-body clusters are highlighted with red lines. (c) Cluster correlation function (CCF) values for the first to sixth two-body clusters of CsPbBr₂Cl at different temperatures. The structural model was created using the VESTA program [50].

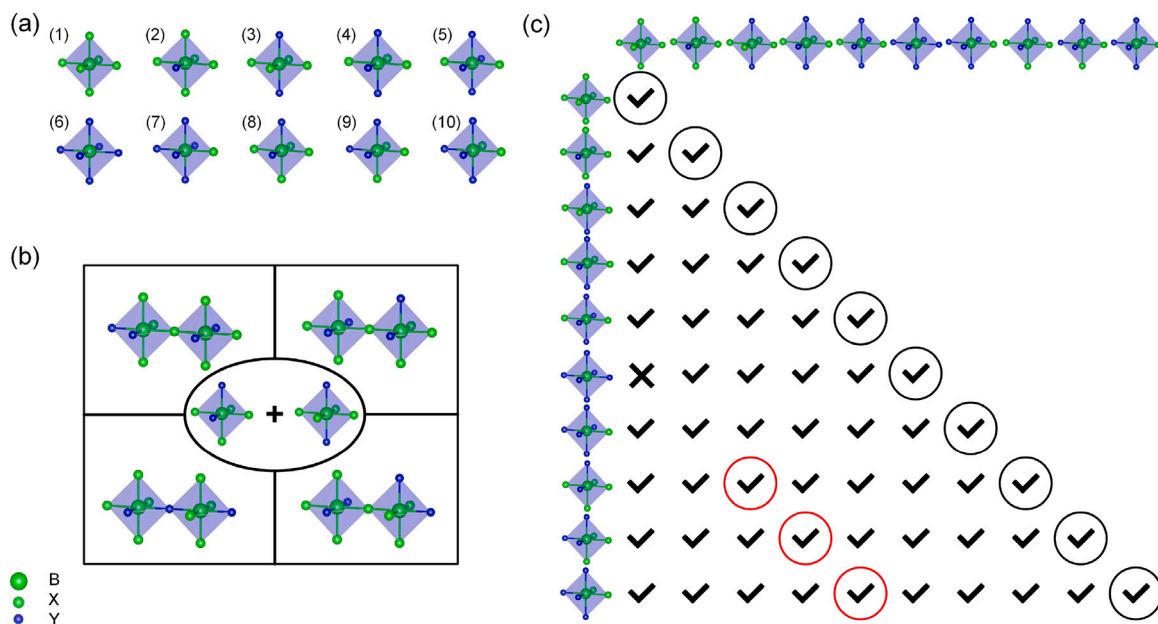


Fig. 2. (a) Type-1 to type-10 inequivalent binary anion substitution patterns in octahedra. (b) Four inequivalent co-vertex matches for type-3 and type-8 octahedra. (c) Octahedra that can be paired by sharing vertices. The symbol “✓” indicates that two octahedra can be paired by sharing vertices, while the symbol “✗” indicates that they cannot. The circles denote the octahedral pairings that occur in the template configuration. A black circle indicates that both octahedra with shared vertices in the template configuration belong to the same type, whereas a red circle indicates that they belong to different types.

3.2. Design of the ACM correlation function and template configurations

To capture the short-range order within octahedra, we first enumerate and distinguish the types of octahedra present within configurations. Ten types of inequivalent binary substitutions for octahedra are identified, as shown in Fig. 2(a). The variations among octahedral types within configurations are reflected in the correlation functions composed of many-body terms in the ACM. Next, when two octahedra share vertices, their relative random arrangement is characterized without distinguishing their specific orientations. For instance, as illustrated in Fig. 2(b), when type-3 and type-8 octahedra share vertices, there are four inequivalent matching scenarios. We assume that all four scenarios

contribute equally to the energy because the elementary occupation of the two-body cluster between the two octahedra does not exhibit any ordered preference (c.f. Fig. 1(c)). Consequently, these scenarios are assigned the same correlation function value.

According to this design, all possible occurrences of paired octahedron clusters within the configuration can be enumerated. As shown in Fig. 2(c), there are a total of 54 possible cases of paired octahedra, excluding the one-shared-vertex matching between type-1 and type-6 octahedra, which is prohibited by the element type restriction. Based on these pairings, the correlation functions for each configuration can be determined by evaluating the matching of octahedra that share vertices. Subsequently, the convex hull points within the set of correlation

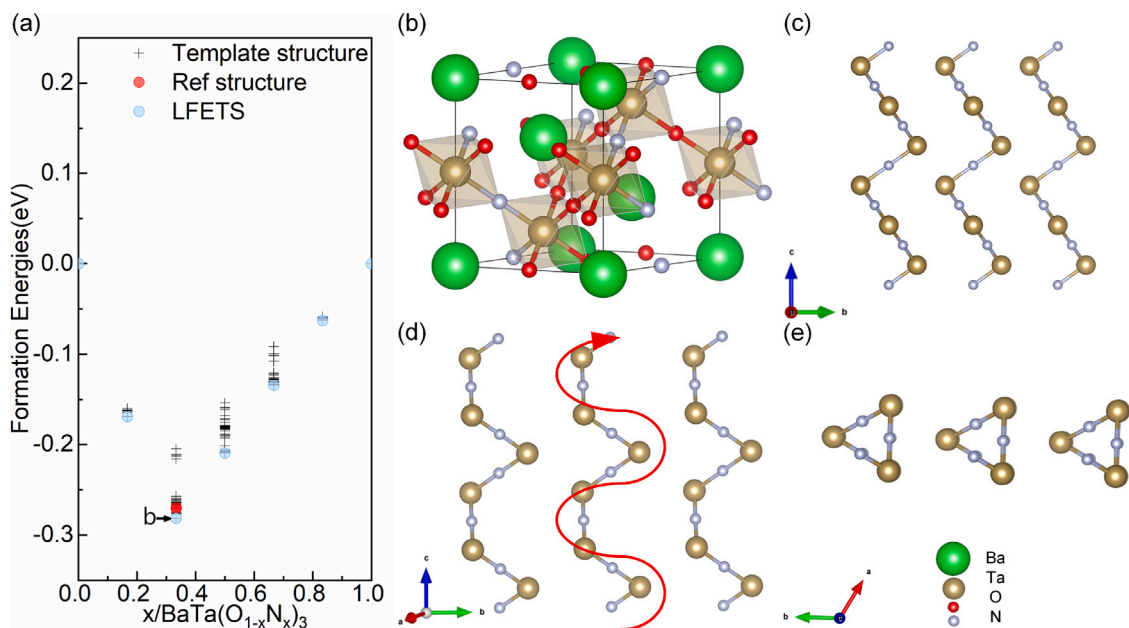


Fig. 3. $\text{BaTa}(\text{O}_{1-x}\text{N}_x)_3$ system (a) The formation energy in the $\text{BaTa}(\text{O}_{1-x}\text{N}_x)_3$ system. The blue points represent the lowest formation energy template structures (LFETS) at various concentrations, while other template configurations are represented by cross symbols. The “b” symbol denotes the b-configuration, which corresponds to the lowest formation energy template structure at 1/3 concentration. The red points indicate the lowest formation energy configurations identified in previous literature [16]. (b) The prototypical structural model of the b-configuration. (c), (d), and (e) show projection diagrams of the orientation of the -N-Ta-N- chain sequence within the b-configuration in three directions.

functions are identified. It is important to note that configurations with fewer non-zero components in their correlation functions are more likely to correspond to convex hull configurations. Specifically, if a correlation function contains only one non-zero component, it is necessarily a convex hull vector, regardless of the cell size used to generate the substitution configurations.

Herein, we define configurations with ACM correlation functions containing only one non-zero component as template configurations. According to the ACM, such configurations are likely to exhibit extreme energy values. The results obtained from enumerated substitution configurations within 8 formula unit (FU) cells indicate that the octahedral pairing situations in template configurations can be categorized into two groups, as illustrated by the circles in Fig. 2(c). The first group, represented by black circles, denotes configurations where both octahedra sharing vertices in the template configuration are of the same type. The second group, represented by red circles, denotes configurations where the shared-vertex octahedra are of two different types. It is common for structures to consist of only one type of octahedron; however, a correlation function can contain only one component in structures comprising type-3 and type-8 octahedra, which corresponds to an antiferromagnet-like distribution. An illustrative diagram is provided for clarity (c.f. Fig. S2). Compared with the number of structures analyzed using an enumerative search, the computational cost is significantly reduced (c.f. Fig. S3). By combining first-principles calculations with template configurations, structures with lower formation energies can be effectively distinguished, thereby improving the screening efficiency.

3.3. Applications in $\text{BaTa}(\text{O}_{1-x}\text{N}_x)_3$ / $\text{RbPb}(\text{F}_{1-x}\text{O}_x)_3$ / $\text{CsPb}(\text{Br}_{1-x}\text{Cl}_x)_3$

To validate the effectiveness of the proposed method, we conducted a stability study on the $\text{BaTa}(\text{O}_{1-x}\text{N}_x)_3$ system using template configurations. The BaTaO_2N system has been extensively studied, as variations in anion sequences can result in intriguing dielectric properties. Determining stable configurations is crucial for understanding the relationship between anion ordering and dielectric properties in this system. Previous studies have explored configurations with “90-degree” characteristics, and the -N-Ta-N- chain sequence in the configuration with the lowest formation energy has been documented

in the literature [16]. Based on the ACM template configurations, which include no more than 4-FU cells, the lowest formation energies of the $\text{BaTa}(\text{O}_{1-x}\text{N}_x)_3$ system at various concentrations are presented in Fig. 3(a). In the 3-FU cells, a more stable b-configuration was identified, as illustrated in Fig. 3(b). Similar to structures reported in previous studies [16], the b-configuration contains only one type of octahedron. However, the connectivity between co-vertex octahedra differs (c.f. Fig. S4), resulting in a distinct arrangement of the N anions in the b-configuration, characterized by a unique triangular helical sequence of the -N-Ta-N- chain (c.f. Fig. 3(d)). The extension directions of these helical chains are parallel to each other without any crossing between chains (c.f. Fig. 3(c)(e)). This new configuration exhibits a lower formation energy, suggesting that the -N-Ta-N- chain sequence prefers such triangular helical arrangements.

Previous studies have conducted a comprehensive and detailed stability analysis of mixed-anion perovskite materials with ABX_2Y stoichiometry (where A and B represent any elements from the periodic table, and X and Y are nitrogen, oxygen, or fluorine) [40]. Most configurations with the lowest formation energy were successfully encompassed within the template configurations, including the arrangement patterns of anions in the SrTaO_2N and RbBiO_2F systems. However, it is noteworthy that the configuration with the lowest formation energy in the RbPbF_2O system does not align with the ACM convex hull template configurations. To verify the general applicability of the ACM, we investigated the stability of the ACM convex hull template configurations with no more than 4-FU cells for the $\text{RbPb}(\text{F}_{1-x}\text{O}_x)_3$ system. The results, as shown in Fig. 4(c), reveal a more stable structure (b-configuration) at a 1/3 concentration compared to the a-configuration reported in the literature. Unlike the b-configuration of the $\text{BaTa}(\text{O}_{1-x}\text{N}_x)_3$ system (c.f. Fig. 3(b)), which contains only one type of octahedron, the b-configuration of the $\text{RbPb}(\text{F}_{1-x}\text{O}_x)_3$ system (c.f. Fig. 4(b)) contains two distinct types of octahedra: type-3 and type-8. In comparison, the a-configuration (c.f. Fig. 4(a)), which also comprises two types of octahedra, has a formation energy 8 meV higher. Additionally, in the b-configuration (c.f. Fig. 4(b)), there are no co-vertex pairings of type-3 and type-3 or type-8 and type-8 octahedra. Instead, the structure exclusively features type-3 and type-8 co-vertex paired octahedra (c.f. small figure in Fig. 4(a)(b)). According to the correlation functions

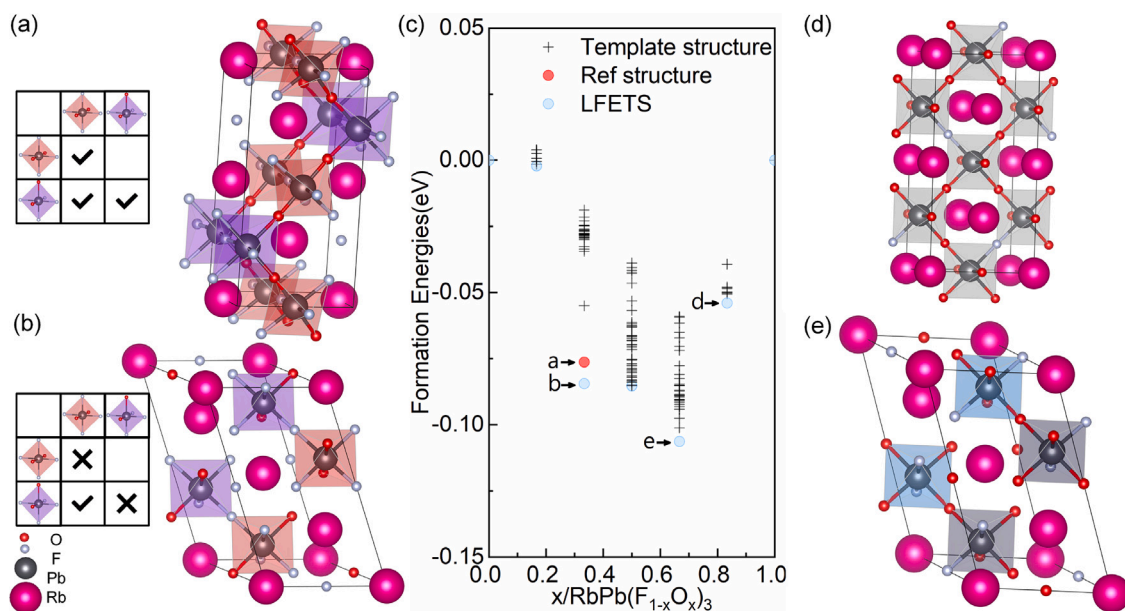


Fig. 4. RbPb(F_{1-x}O_x)₃ system: (a) The a-configuration, identified as the configuration with the lowest formation energy at a concentration of 1/3 in Ref. [40]. (b) The b-configuration, identified as the configuration with the lowest formation energy among the template configurations at a concentration of 1/3. The inset illustrates the type of octahedral co-vertex pairing observed in the a-/b-configuration, with “✓” indicating presence and “✗” indicating absence. (c) The formation energy of the RbPb(F_{1-x}O_x)₃ system. Blue points indicate the lowest formation energy template structures (LFETS) at various concentrations, while other template configurations are represented by cross symbols. Letters “a/b/d/e” denote the corresponding a/b/d/e-configurations. (d) The d-configuration. (e) The e-configuration. Different types of octahedra are distinguished by various colors.

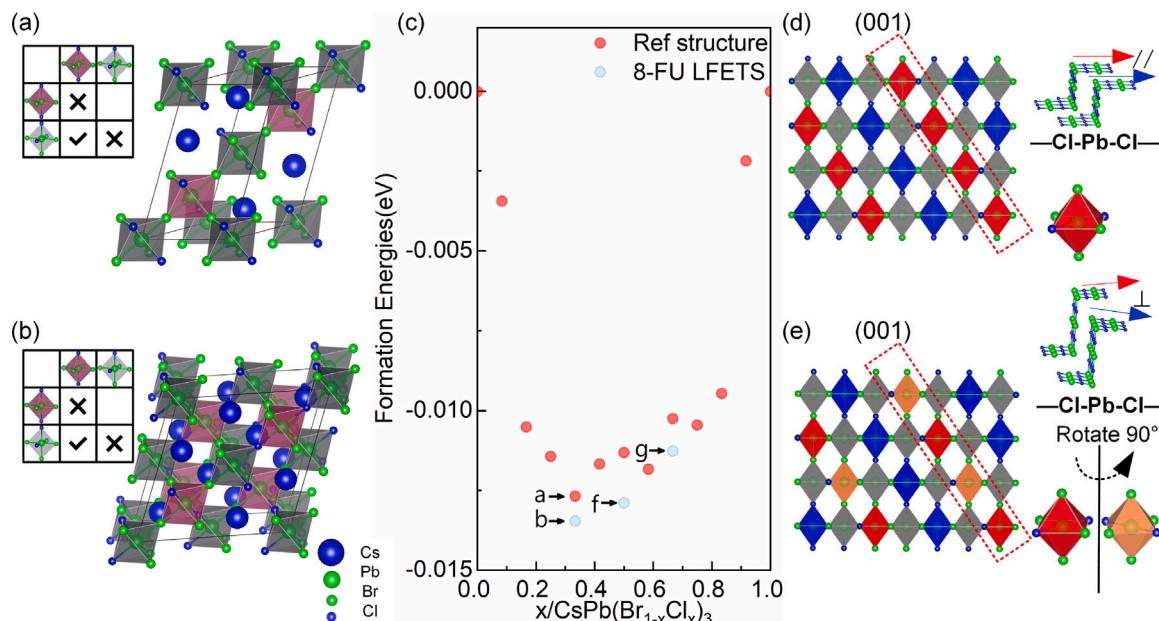


Fig. 5. CsPb(Br_{1-x}Cl_x)₃ system: (a) The a-configuration, identified as the configuration with the lowest formation energy at a 1/3 concentration in previous literature. (b) The b-configuration, identified as the configuration with the lowest formation energy among the template configurations of the 8-FU cells at a 1/3 concentration. Purple and gray colors are used to distinguish octahedra of different types. The inset illustrates the type of octahedral co-vertex pairing observed in the a-/b-configuration, with “✓” indicating presence and “✗” indicating absence. (c) The formation energy of the CsPb(Br_{1-x}Cl_x)₃ system. Blue points represent the LFETS identified at several concentrations in 8-FU cells, while red points represent the lowest formation energy structures found in previous literature at various concentrations [52]. Letters “a/b/f/g” denote the corresponding a/b/f/g-configurations, with prototypical structures of the a- and b-configurations shown in (a) and (b), and prototypical structures of the f- and g-configurations referenced from Fig. S6. (d) and (e) illustrate the stacking modes of octahedra in the a- and b-configurations, respectively. The red, orange, and blue colors represent the three different spatial orientations of the type-3 octahedron in the structure, while gray represents the type-8 octahedron. The inset depicts the relative orientation of the –Cl–Pb–Cl– chain in the a-/b-configuration.

in Section 3.2, the b-configuration has only one non-zero component. Additionally, there is a significant difference in the formation energies between the lowest formation energy template structure (b-configuration) and the next-lowest formation energy template structure at a concentration of $x = 1/3$, which may be attributed to substantial differences in bond angle distortions within the structure (c.f. Fig.

S7). Furthermore, as shown in Fig. 4(c), the RbPb(F_{1-x}O_x)₃ system is found to be more stable at a 2/3 concentration. At this concentration, the formation energy of the e-configuration (c.f. Fig. 4(e)) is 22 meV lower than that of the b-configuration (c.f. Fig. 4(b)) at a 1/3 concentration. This finding highlights that exploring the configuration space at only one concentration is insufficient for a comprehensive

understanding of stability. To gain deeper insights into the stability of mixed-anion perovskite systems, it is necessary to evaluate the stability of configurations across multiple concentrations. The stable structure screening strategy using the ACM enables the identification of more stable structures without imposing concentration-based restrictions, thereby facilitating exploration across a broader concentration range.

In our previous work [52], we determined the formation energies of all substitution configurations within the 4-FU cells using an enumeration method. The configurations with the lowest formation energies at each concentration are represented by red points in Fig. 5(c). To explore potential stable configurations within larger supercells, substitution configurations within the 8-FU cells were screened. With a total of 9,324,883 substitution configurations in the 8-FU cells, performing enumerative first-principles calculations for all configurations is infeasible. It is worth noting that the template configurations based on the ACM constitute less than 0.03% of the total. Among the multiple concentrations covered by these template configurations, we identified some more stable configurations, represented by blue points in Fig. 5(c), specifically the b-, f-, and g-configurations. In both the a- and b-configurations (c.f. Fig. 5(a)(b)), the same type of octahedron is present, and both contain only type-3 and type-8 co-vertex paired octahedrons. The a-configuration (c.f. Fig. 5(a)) features type-3 octahedra with two different orientations, while the b-configuration (c.f. Fig. 5(b)) includes type-3 octahedra with three different orientations. In the a-configuration, the type-3 octahedra with two orientations are staggered and stacked along the [001] direction, resulting in the octahedra within the same layer being oriented in the same direction. In contrast, in the b-configuration, the two orientations of type-3 octahedra are staggered and stacked within the same layer (c.f. Fig. 5(d)(e)). Such a minor difference between the two configurations is reflected in the -Cl-Pb-Cl- chains within the structure. A comparison of the -Cl-Pb-Cl- chains in the a-configuration of the 4-FU cells and the b-configuration of the 8-FU cells reveals that both exhibit a zigzag extension pattern (c.f. small figure in Fig. 5(d)(e)). However, the relative extension directions of the chains in these configurations, as illustrated in Fig. 5(d)(e), are inconsistent. In the a-configuration, the zigzag chains (c.f. small figure in Fig. 5(d)) are parallel to each other, whereas in the b-configuration, the zigzag chains (c.f. small figure in Fig. 5(e)) are perpendicular to each other. This ionic arrangement in the b-configuration further increases the Pb-Br-Pb bond angle distortion within the structure (c.f. Fig. S5). Notably, such anionic sequences in the b-configuration can only be identified in larger supercell substitution configurations. For the f- and g-configurations, it is observed that, unlike the b-configuration, they consist of pairings of two different types of octahedra. Specifically, the f-configuration comprises type-4 and type-9 octahedra (c.f. Fig. S6(a)), while the g-configuration consists of type-5 and type-10 octahedra (c.f. Fig. S6(b)). Based on the correlation functions discussed in Section 3.2, it is evident that only one component is non-zero in all these configurations.

Configurational discrepancies are reflected in the corresponding electronic structures. Specifically, the a- and b-configurations of the $\text{RbPb}(\text{F}_{1-x}\text{O}_x)_3$ system exhibit the characteristics of an indirect bandgap semiconductor, with bandgaps of 1.12 eV and 1.60 eV, respectively. The more stable and symmetric b-configuration exhibited a larger bandgap, with a higher electronic occupied state density of the O atom at the band edge compared to the a-configuration (c.f. Fig. S8(a)(b)). In contrast, the a- and b-configurations of the $\text{CsPb}(\text{Br}_{1-x}\text{Cl}_x)_3$ system exhibit traits of a direct bandgap semiconductor. However, the slight differences in the atomic structures between the a- and b-configurations result in an insignificant variance in their electronic structures (c.f. Fig. S8(c)(d)).

4. Conclusion

In summary, we combined the CE method with the ACM to design rational correlation functions. This approach enables the classification

and ranking of candidate configurations in mixed-anion perovskite alloy systems. To expedite the screening process for stable structures, we prioritized the calculation of template configurations with only one non-zero component of the correlation function. This methodology was validated in three systems: $\text{BaTa}(\text{O}_{1-x}\text{N}_x)_3$, $\text{RbPb}(\text{F}_{1-x}\text{O}_x)_3$, and $\text{CsPb}(\text{Br}_{1-x}\text{Cl}_x)_3$. These validations identified more stable configurations than those reported in previous studies. Among the newly discovered stable configurations, several intriguing phenomena were observed. For instance, in the $\text{BaTa}(\text{O}_{1-x}\text{N}_x)_3$ system, -N-Ta-N- chains exhibited a unique triangular helical arrangement. In the $\text{RbPb}(\text{F}_{1-x}\text{O}_x)_3$ system, the octahedral stacking exhibited characteristics of an antiferromagnet-like distribution. Additionally, in the $\text{CsPb}(\text{Br}_{1-x}\text{Cl}_x)_3$ system, large cells revealed bond angle distortions with a distinctive anionic sequence. Notably, our method significantly reduces computational costs while maintaining transferability and physical interpretability across diverse mixed-anion perovskite systems. This approach greatly enhances the efficiency of exploring stable configurations within extensive compositional and configurational spaces and serves as a valuable reference for investigating anion ordering in mixed-anion perovskite materials.

CRediT authorship contribution statement

Chunwei Zhu: Writing – review & editing, Writing – original draft, Validation, Software, Methodology, Investigation, Formal analysis. **Xiaotong Yan:** Writing – original draft, Visualization, Software. **Yu-Jie Cen:** Validation, Methodology. **Chang-Chun He:** Writing – review & editing, Writing – original draft, Visualization, Methodology, Investigation, Funding acquisition. **Yu-Jun Zhao:** Writing – review & editing, Writing – original draft, Methodology. **Xiao-Bao Yang:** Writing – review & editing, Writing – original draft, Project administration, Methodology, Investigation, Formal analysis, Conceptualization.

Declaration of competing interest

The authors declare that they have no known competing financial interests or personal relationships that could have appeared to influence the work reported in this paper.

Acknowledgments

This work was supported by the NSFC, People's Republic of China (Grant No. 12474228), Guangdong Provincial Key Laboratory of Functional and Intelligent Hybrid Materials and Devices, People's Republic of China (Grant No. 2023-GDKLFIHMD-04), and the Science and Technology Program of Guangzhou, People's Republic of China (Grant No. 202201010090). This work is partially supported by High Performance Computing Platform of South China University of Technology.

Appendix A. Supplementary data

Supplementary material related to this article can be found online at <https://doi.org/10.1016/j.commatsci.2024.113564>. Energy model of CE, designed correlation functions, number of template structures, geometries of stable structures.

Data availability

Data will be made available on request.

References

- [1] S. Kikkawa, S. Sun, Y. Masubuchi, Y. Nagamine, T. Shibahara, Ferroelectric response induced in *cis*-type anion ordered SrTaO_2N oxynitride perovskite, *Chem. Mater.* 28 (5) (2016) 1312–1317, <http://dx.doi.org/10.1021/acs.chemmater.5b04149>.
- [2] A. Kubo, G. Giorgi, K. Yamashita, Anion ordering in CaTaO_2N : Structural impact on the photocatalytic activity. Insights from first-principles, *Chem. Mater.* 29 (2) (2017) 539–545, <http://dx.doi.org/10.1021/acs.chemmater.6b03366>.

- [3] A. Ziani, C. Le Paven, L. Le Gendre, F. Marlec, R. Benzerga, F. Tessier, F. Cheviré, M.N. Hedhili, A.T. Garcia-Esparza, S. Melissen, P. Sautet, T. Le Bahers, K. Takanabe, Photophysical properties of SrTaO₂N thin films and influence of anion ordering: A joint theoretical and experimental investigation, *Chem. Mater.* 29 (9) (2017) 3989–3998, <http://dx.doi.org/10.1021/acs.chemmater.7b00414>.
- [4] A. Kubo, G. Giorgi, K. Yamashita, MgTaO₂N photocatalysts: Perovskite versus ilmenite structure. A theoretical investigation, *J. Phys. Chem. C* 121 (50) (2017) 27813–27821, <http://dx.doi.org/10.1021/acs.jpcc.7b08874>.
- [5] G. Pilania, A. Ghosh, S.T. Hartman, R. Mishra, C.R. Stanek, B.P. Uberuaga, Anion order in oxysulfide perovskites: Origins and implications, *npj Comput. Mater.* 6 (1) (2020) 71, <http://dx.doi.org/10.1038/s41524-020-0338-1>.
- [6] S.D. Young, J. Chen, W. Sun, B.R. Goldsmith, G. Pilania, Thermodynamic stability and anion ordering of perovskite oxynitrides, *Chem. Mater.* 35 (15) (2023) 5975–5987, <http://dx.doi.org/10.1021/acs.chemmater.3c00943>.
- [7] M. Hojamberdiev, R. Vargas, F. Zhang, K. Teshima, M. Lerch, Perovskite BaTaO₂N: From materials synthesis to solar water splitting, *Adv. Sci.* 10 (33) (2023) 2305179, <http://dx.doi.org/10.1002/adv.202305179>.
- [8] J.B. Hoffman, A.L. Schleper, P.V. Kamat, Transformation of sintered CsPbBr₃ nanocrystals to cubic CsPbI₃ and gradient CsPbBr₃I_{3-x} through halide exchange, *J. Am. Chem. Soc.* 138 (27) (2016) 8603–8611, <http://dx.doi.org/10.1021/jacs.6b04661>.
- [9] H. Kageyama, K. Hayashi, K. Maeda, J.P. Attfield, Z. Hiroi, J.M. Rondinelli, K.R. Poeppelmeier, Expanding frontiers in materials chemistry and physics with multiple anions, *Nature Commun.* 9 (1) (2018) 772, <http://dx.doi.org/10.1038/s41467-018-02838-4>.
- [10] N.J. Jeon, J.H. Noh, W.S. Yang, Y.C. Kim, S. Ryu, J. Seo, S.I. Seok, Compositional engineering of perovskite materials for high-performance solar cells, *Nature* 517 (7535) (2015) 476–480, <http://dx.doi.org/10.1038/nature14133>.
- [11] L. Protesescu, S. Yakunin, M.I. Bodnarchuk, F. Krieg, R. Caputo, C.H. Hendon, R.X. Yang, A. Walsh, M.V. Kovalenko, Nanocrystals of cesium lead halide perovskites (CsPbX₃, X = Cl, Br, and I): Novel optoelectronic materials showing bright emission with wide color gamut, *Nano Lett.* 15 (6) (2015) 3692–3696, <http://dx.doi.org/10.1021/nl5048779>.
- [12] D.J. Kubicki, D. Prochowicz, A. Hofstetter, S.M. Zakeeruddin, M. Grätzel, L. Emley, Phase segregation in Cs_xRb_{1-x} and K-doped mixed-cation (MA)_x(FA)_{1-x}PbI₃ hybrid perovskites from solid-state NMR, *J. Am. Chem. Soc.* 139 (40) (2017) 14173–14180, <http://dx.doi.org/10.1021/jacs.7b07223>.
- [13] A. Babayigit, A. Ethirajan, M. Muller, B. Conings, Toxicity of organometal halide perovskite solar cells, *Nat. Mater.* 15 (3) (2016) 247–251, <http://dx.doi.org/10.1038/nmat4572>.
- [14] T. Yang, D. Huang, Z. Wang, F. Li, J. Gong, W. Cui, Y. Hao, X. Kang, Y. Ma, H. Zhang, Y. Sun, Q. Li, Y. He, X. Sun, X. Cui, L. Mao, Manipulating wide-band-gap perovskite compositions via Br sources for highly efficient perovskite/silicon tandem solar cells, *ACS Appl. Energy Mater.* 7 (14) (2024) 5755–5764, <http://dx.doi.org/10.1021/acsaem.4c00822>.
- [15] K. Page, M.W. Stoltzfus, Y.-I. Kim, T. Proffen, P.M. Woodward, A.K. Cheetham, R. Seshadri, Local atomic ordering in BaTaO₂N studied by neutron pair distribution function analysis and density functional theory, *Chem. Mater.* 19 (16) (2007) 4037–4042, <http://dx.doi.org/10.1021/cm0709673>.
- [16] Y. Hinuma, H. Moriwake, Y.-R. Zhang, T. Motohashi, S. Kikkawa, I. Tanaka, First-principles study on relaxor-type ferroelectric behavior without chemical inhomogeneity in BaTaO₂N and SrTaO₂N, *Chem. Mater.* 24 (22) (2012) 4343–4349, <http://dx.doi.org/10.1021/cm302335q>.
- [17] S.H. Porter, Z. Huang, P.M. Woodward, Study of anion order/disorder in RTaO₂N (R = La, Ce, Pr) perovskite nitride oxides, *Cryst. Growth Des.* 14 (1) (2014) 117–125, <http://dx.doi.org/10.1021/cg401230a>.
- [18] H. Wolff, R. Dronskowski, First-principles and molecular-dynamics study of structure and bonding in perovskite-type oxynitrides ABO₂N (A = Ca, Sr, Ba; B = Ta, Nb), *J. Comput. Chem.* 29 (13) (2008) 2260–2267, <http://dx.doi.org/10.1002/jcc.20895>.
- [19] M. Yang, J. Oró-Solé, J.A. Rodgers, A.B. Jorge, A. Fuertes, J.P. Attfield, Anion order in perovskite oxynitrides, *Nature Chem.* 3 (1) (2011) 47–52, <http://dx.doi.org/10.1038/NCHEM.908>.
- [20] J.P. Attfield, Principles and applications of anion order in solid oxynitrides, *Cryst. Growth Des.* 13 (10) (2013) 4623–4629, <http://dx.doi.org/10.1021/cg4011168>.
- [21] L. Clark, J. Oró-Solé, K.S. Knight, A. Fuertes, J.P. Attfield, Thermally robust anion-chain order in oxynitride perovskites, *Chem. Mater.* 25 (24) (2013) 5004–5011, <http://dx.doi.org/10.1021/cm4037132>.
- [22] C.-H. Wang, B.J. Kennedy, A.L. Menezes De Oliveira, J. Polt, K.S. Knight, The impact of anion ordering on octahedra distortion and phase transitions in SrTaO₂N and BaTaO₂N, *Acta Crystallogr. B Struct. Sci. Cryst. Eng. Mater.* 73 (3) (2017) 389–398, <http://dx.doi.org/10.1107/S2052520617001123>.
- [23] M. Ochi, K. Kuroki, Quantifying the stability of the anion ordering in SrVO₂H, *Phys. Rev. B* 102 (13) (2020) 134108, <http://dx.doi.org/10.1103/PhysRevB.102.134108>.
- [24] S. Ninova, U. Aschauer, Surface structure and anion order of the oxynitride LaTiO₂N, *J. Mater. Chem. A* 5 (22) (2017) 11040–11046, <http://dx.doi.org/10.1039/c7ta01873h>.
- [25] Z. Lan, T. Vegge, I.E. Castelli, Theoretical insight on anion ordering, strain, and doping engineering of the oxygen evolution reaction in BaTaO₂N, *Chem. Mater.* 33 (9) (2021) 3297–3303, <http://dx.doi.org/10.1021/acs.chemmater.1c00370>.
- [26] Y. Goto, C. Tassel, Y. Noda, O. Hernandez, C.J. Pickard, M.A. Green, H. Sakaebe, N. Taguchi, Y. Uchimoto, Y. Kobayashi, H. Kageyama, Pressure-stabilized cubic perovskite oxyhydride BaScO₂H, *Inorg. Chem.* 56 (9) (2017) 4840–4845, <http://dx.doi.org/10.1021/acs.inorgchem.6b02834>.
- [27] D. Oka, Y. Hirose, F. Matsui, H. Kamisaka, T. Oguchi, N. Maejima, H. Nishikawa, T. Muro, K. Hayashi, T. Hasegawa, Strain engineering for anion arrangement in perovskite oxynitrides, *ACS Nano* 11 (4) (2017) 3860–3866, <http://dx.doi.org/10.1021/acsnano.7b00144>.
- [28] Z. Wang, X. Wang, X. Luo, P. Gao, Y. Sun, J. Lv, H. Wang, Y. Wang, Y. Ma, Concurrent learning scheme for crystal structure prediction, *Phys. Rev. B* 109 (9) (2024) 094117, <http://dx.doi.org/10.1103/PhysRevB.109.094117>.
- [29] J.M. Sanchez, Cluster expansion and the configurational theory of alloys, *Phys. Rev. B* 81 (22) (2010) 224202, <http://dx.doi.org/10.1103/PhysRevB.81.224202>.
- [30] J.M. Sanchez, Cluster expansions and the configurational energy of alloys, *Phys. Rev. B* 48 (18) (1993) 14013–14015, <http://dx.doi.org/10.1103/PhysRevB.48.14013>.
- [31] J. Sanchez, F. Ducastelle, D. Gratias, Generalized cluster description of multi-component systems, *Phys. A* 128 (1–2) (1984) 334–350, [http://dx.doi.org/10.1016/0378-4371\(84\)90096-7](http://dx.doi.org/10.1016/0378-4371(84)90096-7).
- [32] J.-Z. Xie, X.-Y. Zhou, H. Jiang, Perspective on optimal strategies of building cluster expansion models for configurationally disordered materials, *J. Chem. Phys.* 157 (20) (2022) 200901, <http://dx.doi.org/10.1063/5.0106788>.
- [33] A. Walle, G. Ceder, Automating first-principles phase diagram calculations, *J. Phase Equilibria* 23 (4) (2002) 348–359, <http://dx.doi.org/10.1361/105497102770331596>.
- [34] A. Zunger, S.-H. Wei, L.G. Ferreira, J.E. Bernard, Special quasirandom structures, *Phys. Rev. Lett.* 65 (3) (1990) 353–356, <http://dx.doi.org/10.1103/PhysRevLett.65.353>.
- [35] S.-H. Wei, L.G. Ferreira, J.E. Bernard, A. Zunger, Electronic properties of random alloys: Special quasirandom structures, *Phys. Rev. B* 42 (15) (1990) 9622–9649, <http://dx.doi.org/10.1103/PhysRevB.42.9622>.
- [36] R. Kikuchi, A theory of cooperative phenomena, *Phys. Rev.* 81 (6) (1951) 988–1003, <http://dx.doi.org/10.1103/PhysRev.81.988>.
- [37] A. Zunger, First-principles statistical mechanics of semiconductor alloys and intermetallic compounds, in: P.E.A. Turchi, A. Gonis (Eds.), *Statics and Dynamics of Alloy Phase Transformations*, Springer US, Boston, MA, 1994, pp. 361–419, http://dx.doi.org/10.1007/978-1-4615-2476-2_23.
- [38] Y.-J. Cen, C.-C. He, S.-B. Qiu, Y.-J. Zhao, X.-B. Yang, Determining ground states of alloys by a symmetry-based classification, *Phys. Rev. Mater.* 6 (5) (2022) L050801, <http://dx.doi.org/10.1103/PhysRevMaterials.6.L050801>.
- [39] J. Sivardière, J. Lajzerowicz, Spin-1 lattice-gas model. II. Condensation and phase separation in a binary fluid, *Phys. Rev. A* 11 (6) (1975) 2090–2100, <http://dx.doi.org/10.1103/PhysRevA.11.2090>.
- [40] H.-C. Wang, J. Schmidt, S. Botti, M.A.L. Marques, A high-throughput study of oxynitride, oxyfluoride and nitrofluoride perovskites, *J. Mater. Chem. A* 9 (13) (2021) 8501–8513, <http://dx.doi.org/10.1039/D0TA10781F>.
- [41] G. Kresse, J. Furthmüller, Efficiency of ab-initio total energy calculations for metals and semiconductors using a plane-wave basis set, *Comput. Mater. Sci.* 6 (1) (1996) 15–50, [http://dx.doi.org/10.1016/0927-0256\(96\)00008-0](http://dx.doi.org/10.1016/0927-0256(96)00008-0).
- [42] G. Kresse, J. Furthmüller, Efficient iterative schemes for ab initio total-energy calculations using a plane-wave basis set, *Phys. Rev. B* 54 (16) (1996) 11169–11186, <http://dx.doi.org/10.1103/PhysRevB.54.11169>.
- [43] P.E. Blöchl, Projector augmented-wave method, *Phys. Rev. B* 50 (24) (1994) 17953–17979, <http://dx.doi.org/10.1103/PhysRevB.50.17953>.
- [44] J.P. Perdew, K. Burke, M. Ernzerhof, Generalized gradient approximation made simple, *Phys. Rev. Lett.* 77 (18) (1996) 3865–3868, <http://dx.doi.org/10.1103/PhysRevLett.77.3865>.
- [45] G.L.W. Hart, R.W. Forcade, Algorithm for generating derivative structures, *Phys. Rev. B* 77 (22) (2008) 224115, <http://dx.doi.org/10.1103/PhysRevB.77.224115>.
- [46] C.-C. He, J.-H. Liao, S.-B. Qiu, Y.-J. Zhao, X.-B. Yang, Biased screening for multi-component materials with structures of alloy generation and recognition (SAGAR), *Comput. Mater. Sci.* 193 (2021) 110386, <http://dx.doi.org/10.1016/j.commatsci.2021.110386>.
- [47] A. Van De Walle, Multicomponent multisublattice alloys, nonconfigurational entropy and other additions to the alloy theoretic automated toolkit, *CALPHAD* 33 (2) (2009) 266–278, <http://dx.doi.org/10.1016/j.calphad.2008.12.005>.
- [48] A. Van De Walle, M. Asta, G. Ceder, The alloy theoretic automated toolkit: A user guide, *CALPHAD* 26 (4) (2002) 539–553, [http://dx.doi.org/10.1016/S0364-5916\(02\)80006-2](http://dx.doi.org/10.1016/S0364-5916(02)80006-2).
- [49] A.V.D. Walle, M. Asta, Self-driven lattice-model Monte Carlo simulations of alloy thermodynamic properties and phase diagrams, *Modelling Simul. Mater. Sci. Eng.* 10 (5) (2002) 521–538, <http://dx.doi.org/10.1088/0965-0393/10/5/304>.
- [50] K. Momma, F. Izumi, VESTA 3 for three-dimensional visualization of crystal, volumetric and morphology data, *J. Appl. Crystallogr.* 44 (6) (2011) 1272–1276, <http://dx.doi.org/10.1107/S0021889811038970>.
- [51] X. Xu, H. Jiang, First-principles investigation on anion order, electronic structure and dielectric properties of BaTaO₂N, *J. Mater. Chem. A* 7 (24) (2019) 14583–14591, <http://dx.doi.org/10.1039/c9ta01690b>.
- [52] C. Zhu, X. Yan, Y.-J. Zhao, X.-B. Yang, The stability of CsPb(Br,Cl_{1-x})₃ all-inorganic mixed halide perovskites, *RSC Adv.* 14 (21) (2024) 14894–14903, <http://dx.doi.org/10.1039/D4RA00818A>.